
Article:
Frost, William James orcid.org/0000-0001-5249-1006, Carpenter, Robert and Vallejo Fernandez, Gonzalo orcid.org/0000-0002-4826-1547 (2024) Anisotropy constant of antiferromagnetic Pt50Mn50. Journal of Physics D: Applied Physics. 185003. ISSN 1361-6463

https://doi.org/10.1088/1361-6463/ad2564

Journal of Physics D: Applied Physics

PAPER • **OPEN ACCESS**

Anisotropy constant of antiferromagnetic $Pt_{50}Mn_{50}$

To cite this article: W Frost *et al* 2024 *J. Phys. D: Appl. Phys.* **57** 185003

OPEN ACCESS
IOP Publishing
Journal of Physics D: Applied Physics
J. Phys. D: Appl. Phys. **57** (2024) 185003 (10pp)
https://doi.org/10.1088/1361-6463/ad2564

Anisotropy constant of antiferromagnetic $Pt_{50}Mn_{50}$

W Frost[1,*], R Carpenter[2] and G Vallejo-Fernandez[1]

[1] School of Physics, Engineering and Technology, University of York, Heslington YO10 5DD, United Kingdom
[2] imec, Kapeldreef 75, 3001 Leuven, Belgium

E-mail: william.frost@york.ac.uk

Received 16 October 2023, revised 2 January 2024
Accepted for publication 1 February 2024
Published 13 February 2024

Abstract

We have measured the anisotropy constant of polycrystalline PtMn thin films deposited on different seed layer materials: Pt, Ru and Nb. Values as high as $(2.5 \pm 0.5) \cdot 10^7 \mathrm{erg\,cm^{-3}}$ were achieved for samples deposited on Pt. The films can be crystallised into the antiferromagnetic, face-centred-tetragonal phase on Ru and Pt seed layers at annealing temperatures compatible with back-end-of-line conditions of up to 400 °C for one to three hours. Additionally these antiferromagnetic layers, 8 nm thick, are highly thermally stable with median blocking temperatures above 200 °C. The effect of diffusion on the stoichiometry of the PtMn layers is discussed with regards to the different seed layer materials.

Keywords: antiferromagnetic materials, BEOL compatible materials, antiferromagnetism, exchange bias, PtMn

1. Introduction

Magnetic random-access memory (MRAM) is a promising non-volatile memory for embedded memories due to its lower energy consumption and reduced cell area [1]. Whilst spin transfer torque MRAM (STT-MRAM) is in production for eFlash [2], in order to expand beyond such a niche application it must out-compete static random-access memory. Currently, STT-MRAM switching speeds show a cross-over point for the slowest, L3 cache at around 5 ns [1], however the faster L1/L2 caches below 1 ns remain out of reach [3]. Recent developments in spin orbit torque MRAM (SOT-MRAM) have shown a potential path to these applications, however this is still limited by excessive write currents, as well as the requirement for an in-plane field for deterministic switching [4]. One of the possible routes to enable lower energy and deterministic SOT-MRAM, or even faster STT-MRAM, are antiferromagnetic (*AF*) materials. As a storage layer, antiferromagnets are interesting due to their effectively net-zero magnetic moment, high magneto-crystalline anisotropy ($>10^7\,\mathrm{erg\,cm^{-3}}$) and an attempt frequency ($>10^{11}\,\mathrm{1\,s^{-1}}$) [5–8]. Such characteristics are expected to lead to lower write currents, higher thermal stability, better external stray-field robustness and faster reversal dynamics.

One of the key requirements for embedded memory is compatibility with back end of line (BEOL) processes, which are required for the integration of the MRAM cell into the Complementary metal-oxide-semiconductor device arrays. These processes can reach temperatures of up to 400 °C. However, this temperature cannot be exceeded due to diffusion of Cu from the contact layers, introducing a temperature window, or thermal budget. This strict requirement defines a narrow category of compatible materials. The primary material investigated to date, $IrMn_x$ [9–11], shows significant degradation when annealed above 300 °C due to Mn diffusion into the adjacent ferromagnetic and seed layers [12]. The composition of IrMn varies away from the stoichiometric $IrMn_3$ to increase

* Author to whom any correspondence should be addressed.

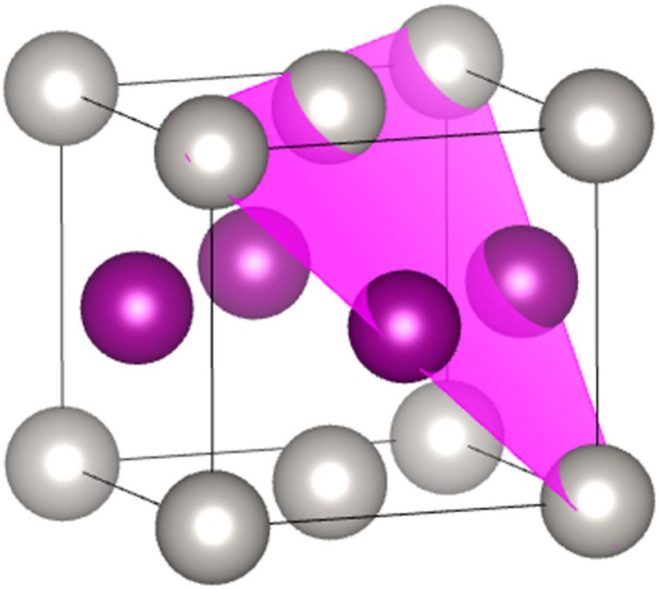

Figure 1. The $L1_0$ phase of PtMn, where silver are Mn and purple are Pt with the (111) plane highlighted.

the anisotropy of the material, up to $IrMn_5$ [13]. There are approaches where this diffusion can be compensated [14, 15], or even blocked [16]. However, even with this process engineering, the maximum temperature possible before degradation of properties is observed is ∼350 °C. Additionally Ir is exceptionally rare and expensive, extracted as 1%–5% of a typical platinum mining yield. Therefore an alternative material must be used.

PtMn alloys gained significant interest in the 2000 s as an alternative material for thermal MRAM [17]. The optimisation and crystallisation of equiatomic PtMn from the as-deposited, disordered, face-centred cubic (fcc) phase to the highly anisotropic face-centred-tetragonal (fct) $L1_0$ phase have been previously investigated by a number of groups, e.g. Ranjbar *et al* [18, 19], but very little published data is available on the anisotropy constant, K, of this material. The $L1_0$ phase is shown in figure 1, with the (111) plane highlighted for reference. Kato *et al* [20] reported a value of $8.0 \cdot 10^6$ erg cm^{-3} for MBE grown films. However, for all applications polycrystalline sputtered thin films with grain sizes circa 8–10 nm are used.

In this work, we have measured the anisotropy constant of PtMn thin films deposited by sputtering on a range of seed layers using a technique we have described previously [21]. The method, which will be described later, is based on a measurement of the distribution of blocking temperatures in exchange bias systems. Exchange bias is observed when a ferromagnetic (F) layer is grown in direct contact with an antiferromagnet. The exchange interaction across the *F/AF* interface results in a shifted hysteresis loop along the field axis when the system is field cooled.

Three materials were chosen for their lattice matching properties to the bulk-fct phase of PtMn: hcp Ru and fcc Nb and Pt. These materials have lattice mismatches to the PtMn{111} planes of −4.7%, −14.8% and +1.0% respectively and should introduce a wide range of both compressive and tensile strains on the PtMn, which are expected to affect the effective value of the anisotropy constant [22]. For instance, using Nb seed layers beneath PtMn is expected to induce more interfacial defects or lead to a change in the growth mechanism due to such a significant lattice parameter mismatch at the interface. Such changes in the lattice should result in variations in the magneto-crystalline anisotropy and affect both the exchange bias field and the thermal stability of the *AF* spin ordering in exchange bias systems.

2. Materials and methods

The samples were deposited onto thermally oxidised 300 mm Si-(001) substrates using a cluster magnetron sputtering tool (Canon-Anelva, EC7800). Due to the difference in sputtering rates of the two component metals, the composition of the PtMn target was $Pt_{43.5}Mn_{56.5}$. This ensured the on-wafer composition was equiatomic $Pt_{50}Mn50$, as was confirmed through Rutherford backscattering spectroscopy using a NEC 6SDH Pelletron accelerator with a range of H+ acceleration voltages from 500 keV to 3.5 MeV. Three seed layers of X = (Ru, Nb and Pt) were grown in a multilayer of TaN(2)/Ta (5)/X (10)/PtMn (8)/ $CoFeB_{20}$ (2.5)/Mg (0.65)/Ta (5), where the numbers in brackets are the thicknesses of the layers in nanometers. The composition of the CoFeB was $Co_{20}Fe_{60}B_{20}$. To crystallise the PtMn layers into the desired highly anisotropic tetragonal phase with *AF* spin ordering, the samples were annealed and subsequently field cooled at 50 kOe for 90 min (TEL MRT5000) in temperature steps of 25 °C from (325 to 475) °C for Ru seed layers and (325–425) °C for Nb and Pt seed layers. The combinations of the temperatures and the applied field act as the activation energy for the phase transformation and the thermal activation energy to align the antiferromagnetic spins. The orientation of the antiferromagnetic spins in the PtMn is controlled by direct exchange from the ferromagnetic CoFeB during the thermally active stage and therefore the applied field must be sufficiently large to saturate the F layer [23] . Additionally, interfacial *AF* spins are reported to lead to a setting-field dependence of the exchange bias [24]. Therefore, a field of 50 kOe was selected as it was sufficient to saturate both effects.

The magnetic properties were characterised using KLA-Microsense Model 10 and LakeShore 8600 vibrating sample magnetometers with sensitivities better than 1×10^{-6} emu and a field precision of 0.1 Oe. The temperature was varied in the range 100–498 K to allow for determination of the distribution of blocking temperatures in the samples. These measurements can be used to calculate the effective anisotropy constant of the PtMn layers [21]. The measurement procedure to obtain such curves has been described in detail previously [5]. Briefly, the reproducible setting of the *AF* layer is achieved by heating the sample in the presence of a magnetic field large enough to saturate the F layer. In our case a field of 10 kOe was used with

the system held in this configuration for 90 min given the logarithmic dependence of the setting process [25]. The samples were then cooled to room temperature and the field reversed so that the F layer was saturated in the opposite direction to that used during the setting process. At this point the temperature was increased to a value T_{act} for 30 min still with the field applied in the negative direction. The samples were finally cooled to room temperature and the hysteresis loop measured. By varying the value of T_{act} in a systematic way the distribution of blocking temperatures in the AF can be mapped. As a result the hysteresis loop of the F layer shifts from negative to positive field values. The value of the loop shift $H_{\mathrm{ex}}(T_{\mathrm{act}})$ at any given activation temperature T_{act} is given by

$$H_{ex}\left(T_{\mathrm{act}}\right) \propto -\int_{V_{\mathrm{c}}(T_{\mathrm{meas}})}^{V_{\mathrm{act}}(T_{\mathrm{act}})} f(V)\,\mathrm{d}V + \int_{V_{\mathrm{act}}(T_{\mathrm{act}})}^{V_{\mathrm{set}}(T_{\mathrm{set}})} f(V)\,\mathrm{d}V \quad (1)$$

where $V_{\mathrm{c}}(T_{\mathrm{meas}})$ is the critical volume that is thermally stable at the temperature of measurement, $V_{\mathrm{act}}(T_{\mathrm{act}})$ is the critical volume being activated at the activation temperature T_{act} and $V_{\mathrm{set}}(T_{\mathrm{set}})$ is the largest volume that can be set during the field setting process. $f(V)$ is the distribution of energy barriers in the AF layer which is controlled by both the distribution of grain volumes in the AF layer and the anisotropy constant of the material K_{AF}. Assuming K_{AF} is uniform across grains, the distribution of energy barriers reduces to the distribution of volumes in the system. The values of V_{c}, V_{act} and V_{set} can be calculated as follows

$$V_{\mathrm{c}}\left(T_{\mathrm{meas}}\right) = \frac{\ln\left(10 f_0\right) k_B T_{\mathrm{meas}}}{K_{AF}\left(T_{\mathrm{meas}}\right)} \quad (2)$$

$$V_{\mathrm{act}}\left(T_{\mathrm{act}}\right) = \frac{\ln\left(1800 f_0\right) k_B T_{\mathrm{act}}}{K_{AF}\left(T_{\mathrm{act}}\right)} \quad (3)$$

$$V_{\mathrm{set}}\left(T_{\mathrm{set}}\right) = \frac{\ln\left(5400 f_0\right) k_B T_{\mathrm{set}}}{K_{AF}\left(T_{\mathrm{set}}\right)} \quad (4)$$

where K_{AF} is the anisotropy constant of the PtMn layer. The factor 10 in equation (2) arises from the relaxation time being equal to the measurement time. Similarly, the factors 1800 and 5400 in equations (3) and (4) are due to the those being the times used to thermally activate and set the AF layer, respectively. Finally, the temperature dependence of the anisotropy was was taken as [5]

$$K(T) = K(0)\left(1 - \frac{T}{T_N}\right). \quad (5)$$

For the crystallographic analysis, a Rigaku SmartLab x-ray diffractometer (XRD) was used with a 9 KW rotating anode Cu-K$_\alpha$ source and a Ge(220) 2-bounce monochromator with an angular resolution $<0.01°$. Cross-section (scanning) transmission electron microscope ((S)TEM) images were obtained using an FEI Titan^3 G2 60–300 with a 200 kV accelerating voltage achieving a probe size of $\sim$0.07 nm. Composition mapping was measured with a Thermofisher Super-X EDS with a minimum resolution of $\sim$0.1 nm.

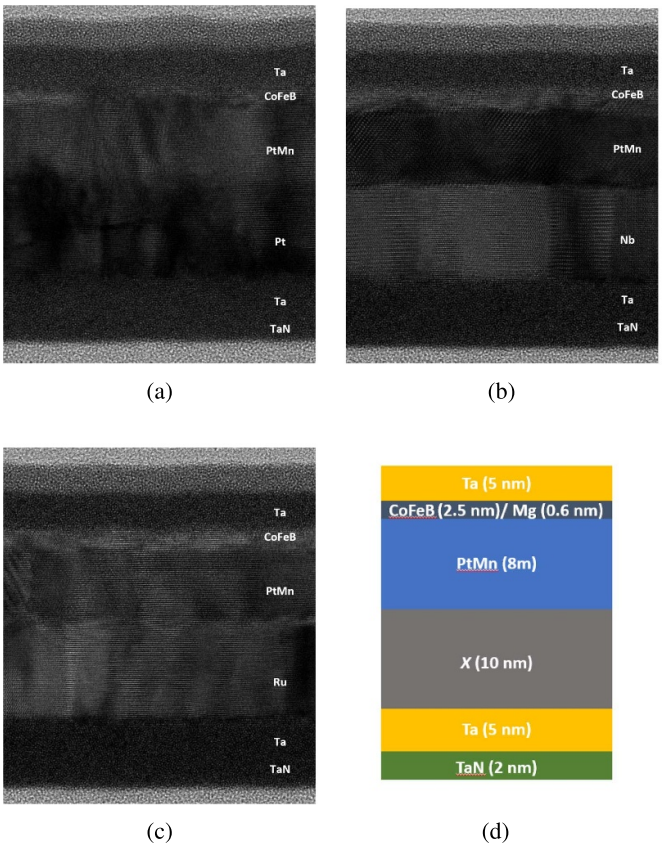

Figure 2. Cross-section TEM micrographs of the multilayers with (a) Pt, (b) Nb and (c) Ru seed layers annealed at 425 °C.

3. Results and discussion

3.1. Microscopy and spectroscopy

Figures 2(a)–(c) show the cross-sectional TEM micrographs for the samples with Pt, Nb and Ru seed layers annealed at 425 °C. From figure 2(a) it is clear that the close lattice match between Pt and PtMn leads to a textured growth with no large dislocations at the interface and low roughness. The small lattice mismatch of +1% and mutual solubility of the components of the Pt, PtMn and CoFeB layers enabled diffusion and intermixing. This is shown in figure 3(a) by an EDX line trace of the multilayer shown in figure 2(a). The clear tail on the lower side of the Mn profile, shown in dark green, indicates diffusion of the Mn into the PtMn. This is not surprising as Mn is highly mobile and prone to diffusion, especially at elevated temperatures, and PtMn has a varied phase diagram with a wide range of compositions [26–28]. This is a major factor in the incompatibility of IrMn alloys with BEOL processing, where their properties are destroyed by diffusion at over 350 °C [10].

Mn diffusion will affect the PtMn composition, potentially affecting the AF ordering. In this case a Mn concentration, and therefore composition, gradient was formed through the PtMn and Pt layers. The concentration of the Mn drops through the Pt layer from 13% at the interface to 0% once the Ta layer is reached. At the Pt interface a sharp change was observed in the

line scan and as such the two layers have not completely intermixed and a clear interface is still present. Additionally, at the PtMn/CoFeB interface the ratio of Pt:Mn remains roughly 1:1, indicating that the desired stoichiometry is maintained at the interface. Hence, the fct structure with AF magnetic ordering required to create an exchange bias is present, as discussed in section 3.3. It is possible that the Mn diffusion gradient decreased the lattice mismatch between the Pt and PtMn layers in order to lower the interfacial energy. This potentially improved the crystallinity and decreased the roughness of the PtMn film at the interface with CoFeB and ensured that a bulk-like lattice was reached at the *AF/F* interface. However, in order for these two criteria to be true, a minimum thickness, t_{min}, of PtMn will be required to maintain the necessary composition at the *AF/F* interface and for the relaxation of the lattice constant toward the bulk, or a suitable level of lattice strain for the *AF* ordering to still be present and complete. There is also a level of strain from the capping layer and the *F* layer above the PtMn, competing with the strain from the seed layer. In this work the layer thickness, *t*, was 8 nm. It is possible that a thinner layer could be used, but the EDX line-scan shows a clear gradient through at least 5 nm of the layer, indicating a possible value of t_{min}.

Figures 3(a) and 4(c) also show there was a distribution of the Fe and, to a lesser extent, Co intensity outside the CoFeB layer. A broad, distributed peak in the two distributions is at its maximum at the interface of the PtMn and the Pt, suggesting that the magnetic-layer ions migrated down grain boundaries in the PtMn layer. Similar behaviour has been observed in stainless steels [29]. These ions then accumulated at the Pt surface and diffused slowly into the Pt layer as indicated by the tail of the distribution. This may be an attempt by the lattice to reduce the interface energy due to mismatches. Figure 3(a) also shows significant diffusion of the Ta throughout the multilayer, from both the seed and capping layers. The distribution is uniform throughout the stack indicating the Ta is soluble in each layer. The presence of Ta in magnetic layers will act to poison the *AF* and *F* ordering and the magnetic properties are discussed in section 3.3.

For the Nb seed layer, a similarly high quality growth is shown in figure 2(b) and well oriented and crystalline seed and PtMn layers were observed. Figure 3(b), however, shows that the Nb was a far superior diffusion barrier than the Pt seed layer with respect to several elements. Ta diffusion from the bottom layer is heavily suppressed compared to figure 3(a) and the Fe and Co distributions do not penetrate the Nb. Instead these species were more intensely concentrated at the Nb/PtMn interface. Furthermore the Mn diffusion from the PtMn to the seed layer is reduced, with a much narrower distribution outside of the PtMn layer. With Nb present there is a deeper diffusion of the Pt into the seed layer than of the Mn, although it is difficult to distinguish between an enhancement in the diffusion of Pt and a suppression of the diffusion of Mn. However, the preference for diffusion of Pt increased intermixing and the formation of a PtNb alloy is observed, as shown in figure 4(d) and is discussed later in figure 5(b). Pt is observed even below the Nb layer in the Ta seed, and as such the composition will once again be off-stoichiometric in the PtMn layer, in a manganese rich form. This change in stoichiomentry will have different effects to that observed in the other seed layers, as discussed in section 3.3.

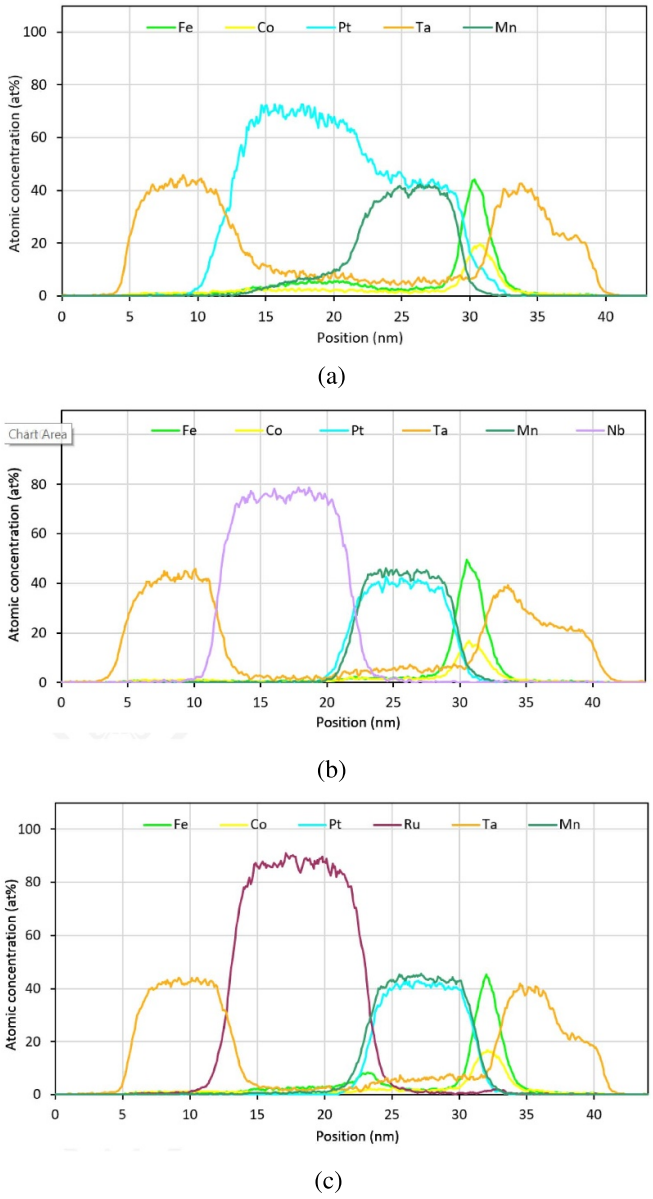

Figure 3. EDX linescans for the samples with (a) Pt, (b) Nb and (c) Ru seed layers annealed at 425 °C to show the elemental diffusion in each layer.

In the samples with a Ru seed layer an interesting combination of the two behaviours was observed, as shown in figure 3(c) and the associated maps in figures 4(g)–(i). There is again a significant diffusion of the Fe and Co, however the Fe very clearly moves through the grain boundaries of the Ru seed layer. From both figures there is also a large amount of Fe stopped at the Ru/PtMn interface and the diffusion through the grain boundaries is much slower. Once the Fe has penetrated the Ru layer down these boundaries, it disperses evenly once more through the Ta underlayer. For a Ru seed layer the Mn diffusion is also reduced compared to the sample with a Pt seed layer, however there is slight preference for Mn over Pt

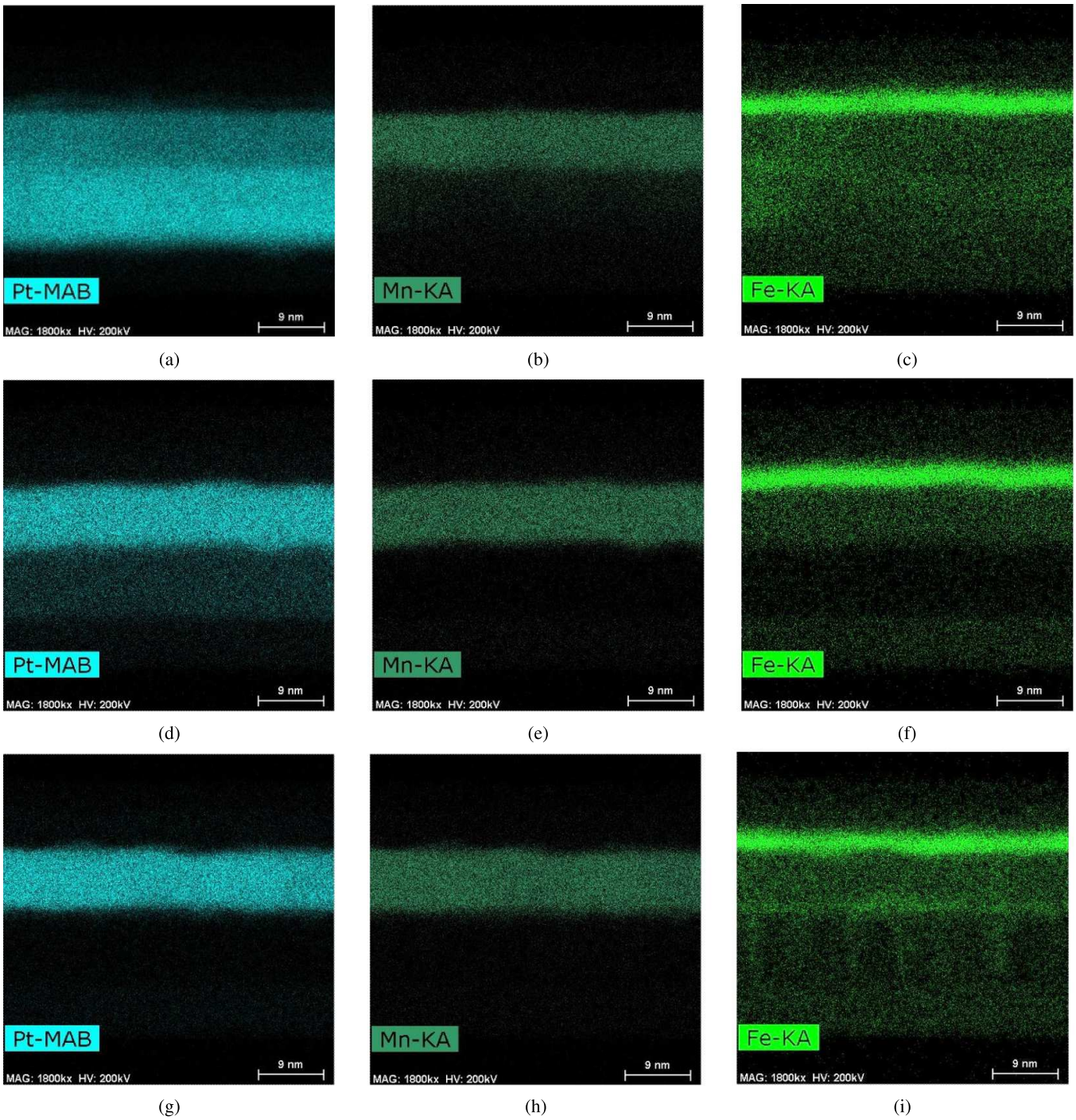

Figure 4. EDX maps of the Pt, Mn and Fe for the samples with (a), (b), (c) Pt, (d), (e), (f) Nb and (g, h (i) Ru seed layers annealed at 425 °C to show the elemental diffusion in each layer.

diffusion. The Ru is also much more effective in preventing Ta diffusion than Pt, like Nb. This will once again affect the stoichiometry of the PtMn layers, although in this case creating a Pt rich, rather than Mn rich, environment.

3.2. Crystallography

The out-of-plane XRD data for the three seed layers are shown in figure 5. The multilayers with Pt seed layers are shown in figure 5(a) and a good lattice match between the two layers is evident. The Mn diffusion shown in figure 3(a) acts to relieve the strain between the two layers at the interface, reducing the lattice mismatch from the bulk values and the two lattices form a single, convoluted Bragg peak, as shown in the figure. However, a shift in the single peak location is observed when the annealing temperature reaches 425 °C and the peak location shifts from the fcc- to fct-(111) location for PtMn.

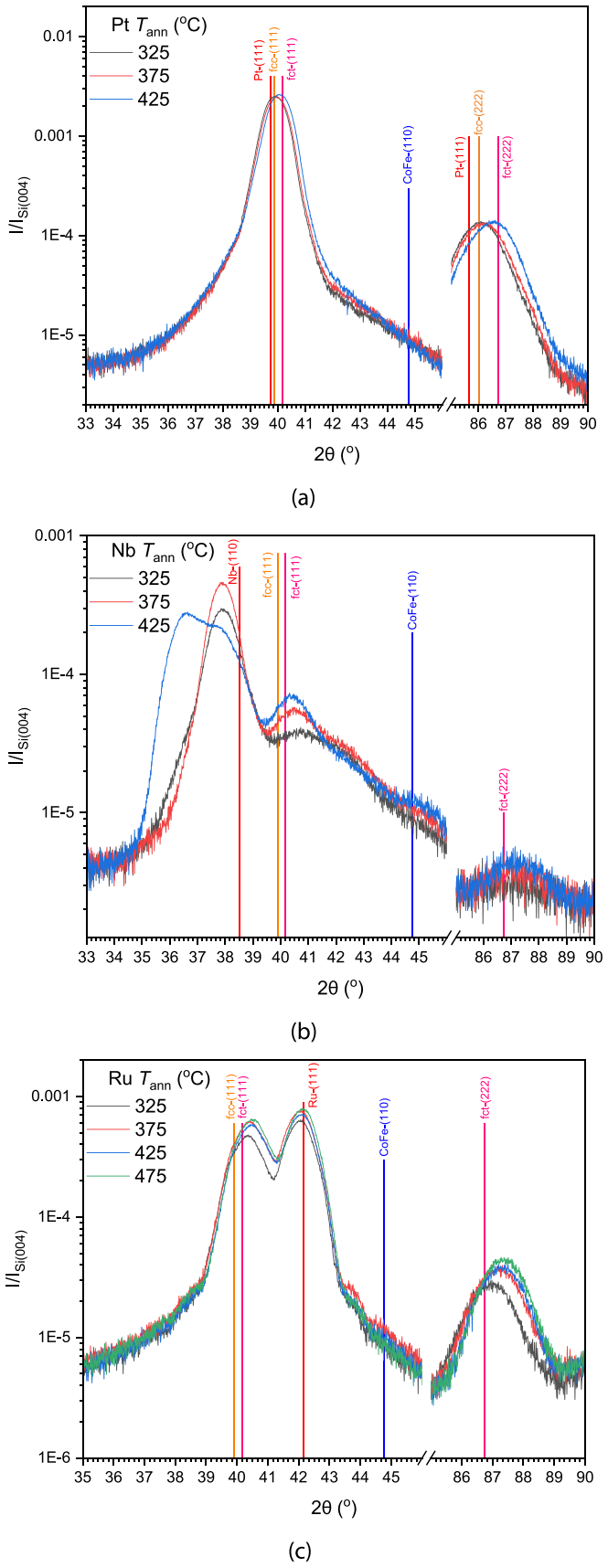

Figure 5. Out-of-plane $\theta - 2\theta$ scans of PtMn/CoFeB bilayers with a (a) Pt, (b) Nb and (c) Ru seed layer after annealing for 1 h at a range of temperatures. Major peak locations are labelled, and the fcc and fct phases of PtMn shown.

Similar significant changes in crystallography are shown for samples based on Nb and Ru seed layers in figures 5(b) and (c) respectively. For the case of Nb seed layers the strain is, however, compressive, with the PtMn-{111} peak shifted by 1.4% for the sample deposited at 325 °C. As the annealing temperature is increased the strain from the bulk value relaxes to 0.44%. However, an additional change is observed in the Nb peak, away from any bulk reflection for elemental Nb. This agrees with the Pt diffusion seen in the EDX data in figure 3(b) and a PtNb alloy may be forming with a highly distorted lattice. The peak is composed of two distributions, implying a mixing of phases within the Nb seed layer. This will result in a mixed seed layer for the PtMn growth and may lead to inconsistencies in the *AF* properties across the bulk of the film. This is also indicated by the low intensity of the normalised reflection when compared to the PtMn layers with a Pt or Ru seed layer.

For the Ru seed layer systems shown in figure 5(c) the PtMn is deposited in a tensile-strain state, with the shift from the highly sensitive bulk, fct {222} position increasing from 0.35% to 0.73% as the annealing temperature increases. There is a significant increase in the intensity of the {111} reflection as the temperature exceeds 375 °C indicating a large increase in crystallinity.

3.3. Magnetic data

Figures 6(a)–(c) show the in-plane *M*-*H*-loops for all of the samples. Figure 6(a) shows the hysteresis loops for the samples with Pt seed layers. The key parameters from the hysteresis loops are presented in table 1 for ease of comparison. The samples annealed at (325 & 375) °C have similar loop shapes and moderate loop shifts of (320 & 380) Oe respectively. For the sample annealed at 425 °C this drops to 210 Oe and a large change in the loop shape is observed. The squareness drops from >0.9 to 0.8 with a significant loop canting. This indicates a move away from a domain nucleation and propagation controlled reversal mechanism, to one dominated by domain wall pinning.

This has two possible origins. Firstly, it could be due to an increase in interfacial roughness due to intermixing and the inclusion of large pinning sites in the ferromagnetic layer. From the cross section and EDX mapping data in figure 3 this seems unlikely as low-roughness interfaces are observed and no significant diffusion into the CoFeB layer occurs. It is therefore more likely that the change in reversal comes from an increase in the anisotropy of the pinning PtMn layer. This inverse trend of decreasing H_{ex} with increasing K is observed in other systems such as IrMn alloys [13].

A similar trend is observed for the samples grown on Ru seed layer, as shown in figure 6(c). The increasing annealing temperature acts to improve the properties of the *AF* layer, due to crystallisation and phase transformation. As the temperature increases the canting of the loop gets more pronounced and the loop squareness decreases. This indicates an increase in the anisotropy of the PtMn layer, as in the Pt seed layer based samples.

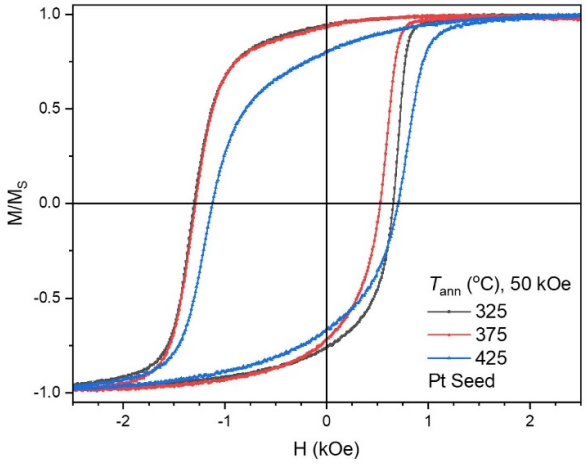

(a)

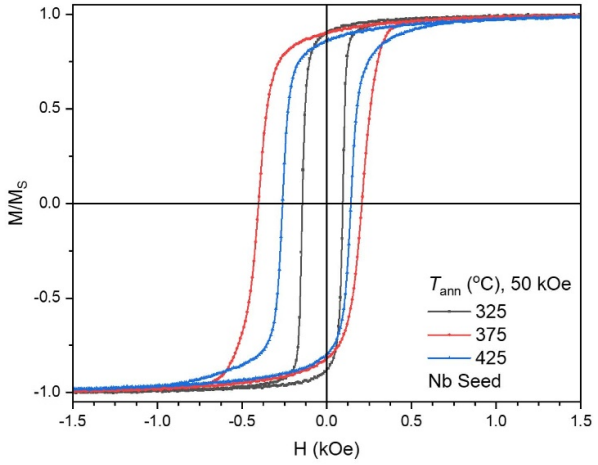

(b)

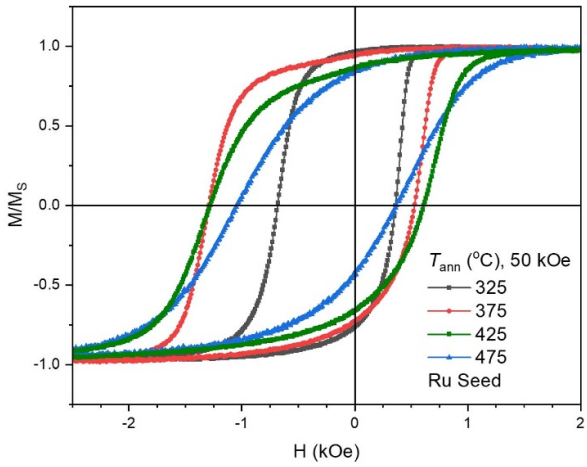

(c)

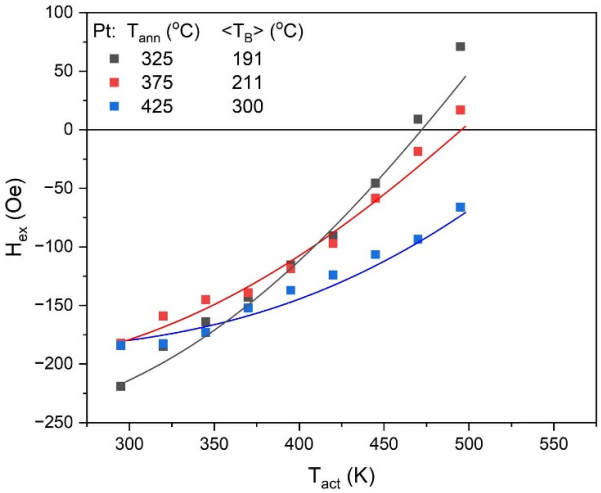

(d)

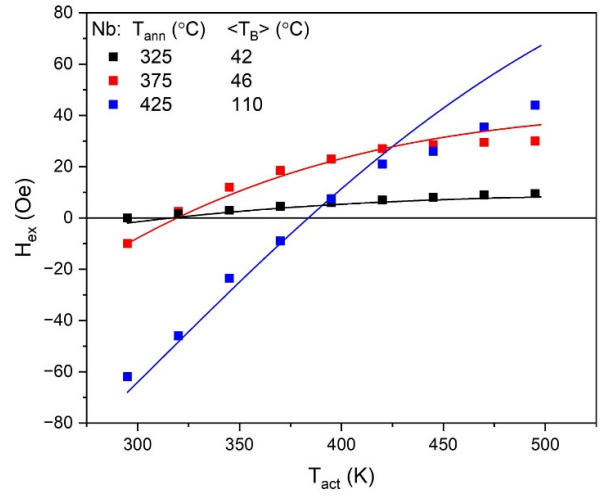

(e)

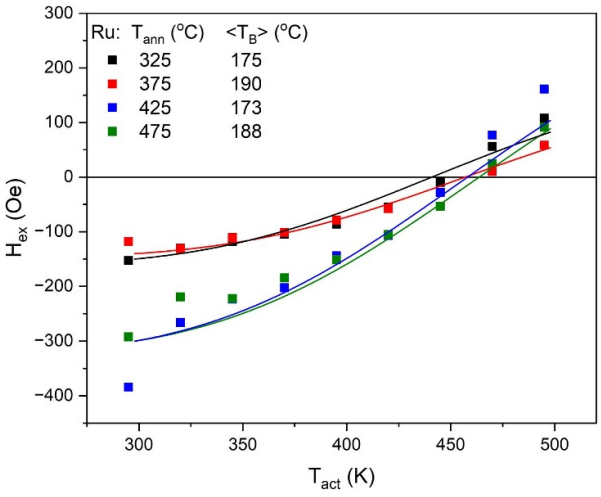

(f)

Figure 6. Hysteresis loops of PtMn/CoFeB samples with seed layers of (a) Pt, (b) Nb and (c) Ru, after annealing for 1 h in a 50 kOe field at increasing temperatures from 325 to 425 °C and additionally 475 °C for the sample wit ha Ru seed layer. (d), (e) and (f) The corresponding blocking curve measurements for the samples and fits according to equation (1) to determine the average blocking temperature, $< T_B >$ and subsequently the anisotropy of the PtMn layer, K_{AF}.

Table 1. Comparison table of key results of hysteresis loop measurements for the samples with all seed layers.

Seed	T_{ann} (°C)	H_c (Oe) (±5)	H_{ex} (Oe) (±5)	Squareness (±0.05)
Pt	325	980	325	0.95
	375	910	380	0.90
	425	915	210	0.80
Nb	325	120	25	0.90
	375	305	95	0.90
	425	205	60	0.85
Ru	325	525	160	0.95
	375	915	385	0.95
	425	945	335	0.85
	475	705	345	0.85

Table 2. The summary of blocking curve measurements to determine K_{AF} for PtMn.

Seed	T_{ann} (°C)	D_m (nm) (±0.5)	σ (±0.05)	K_{AF} ($\times 10^7$ erg cm^{-3}) (±20%)
Pt	325	6.0	0.33	1.8
	375	6.0	0.33	1.8
	425	6.0	0.33	2.5
Nb	325	6.5	0.34	0.37
	375	6.5	0.34	0.38
	425	6.5	0.34	0.70
Ru	325	7.2	0.18	0.85
	375	7.2	0.18	0.90
	425	7.2	0.18	0.90
	475	7.2	0.18	0.92

Nb seed layers lead to a very small exchange bias in the multilayer, up to only 60 Oe, despite the PtMn looking well ordered and crystalline in figure 2(b). A small change in loop shape is also observed at the highest annealing temperature, but the effect is limited beyond a drop in H_{ex}. This reduced loop shift is probably due to the significant lattice mismatch between Nb and PtMn which limits the formation of the highly anisotropic PtMn *AF* phase. Furthermore the diffusion Pt from the PtMn layer into the Nb seed layer may lead to the formation of a PtNb alloy, as mentioned earlier, which could negatively affect the composition of the alloy.

This was investigated further by measuring the distribution of blocking temperatures for each sample shown in figures 6(d)–(f), the main results and parameters of which are shown in table 2. The solid lines in the figures are calculated fits using equation (1). Inevitably certain assumptions had to be made. Firstly, the grain size distribution within the films is unknown. We have used Scherrer analysis [30] of the broadening of the (222) PtMn reflection to estimate the crystallite size within the films. The crystallite size is useful for this calculation compared to a grain size as it gives a volume of crystal ordering and therefore of uniform magnetic order. This yielded values of (6.0 , 6.5 and 7.2) nm for the Pt, Nb and Ru based samples, respectively. We have also compared these values to the granular structure observed in several TEM cross section images for each sample and the values agree within error $<10\%$, implying that the crystallite and mean grain sizes, D_m, are the same. It is important to note that for the complete analysis presented a median volume fraction is required, not the mean grain diameter. As such a significant additional error is introduced. The Néel temperature for the films was taken as the bulk value of 970 K [26] and the attempt frequency for the antiferromagnet as $2.1 \cdot 10^{12}\,\mathrm{s}^{-1}$ [6] leaving only the standard deviation of the lognormal distribution of grain sizes, σ, and the desired value K_{AF} as floating parameters. The value of f_0 is taken from the value for IrMn and as such comes with a significant uncertainty. The solid lines in figures 6(d)–(f) are calculated fits using equation (1). There is good agreement between the experimental data and the theoretical fits calculated as described above. The parameters used to fit the data in figures 6(d)–(f) are summarised in table 2.

The data confirm that a composition change has taken place at elevated annealing temperatures of 425 °C. The increase in anisotropy is related to the peak shifts in figure 5, confirming that a phase transformation to the desired fct phase has at least

partially occurred. Furthermore the value of $2.5 \cdot 10^7\,\mathrm{erg\,cm^{-3}}$ obtained for the sample with a Pt seed layer is very high, comparable to that reported for IrMn at $2.9 \cdot 10^7\,\mathrm{erg\,cm^{-3}}$. A significantly higher value of K_{AF} is obtained for the samples deposited on a Ru and Pt seed layer compared to samples with a Nb seed layer. This is probably the reason for the rounder hysteresis loops obtained for these systems compared to the hysteresis loops measured for the Nb based samples. A higher anisotropy can increase the degree of domain wall pinning in the CoFeB layer resulting in rounder hysteresis loops [15].

4. Conclusions

We have shown that the crystallisation of PtMn thin films into the anisotropic $L1_0$ phase was achieved by annealing at temperatures up to, and above, BEOL conditions enabling median blocking temperatures above 200 °C. This is well in excess of the temperatures required to meet auto-grade-1 applications (−40 °C to 150 °C) [31]. A significant increase in anisotropy was observed with increasing annealing temperature, especially in samples with a Pt seed layer where the value of $K_{AF} = 2.97 \cdot 10^7\,\mathrm{erg\,cm^{-3}}$. EDX, TEM and XRD have shown that recrystallisation into a highly ordered system occurred. However there is significant diffusion regulated choice of material for the seed layer. Interestingly, Fe has been found to migrate through PtMn with ease, and to congregate at the grain boundaries of a columnar Ru seed layer. A full phase transformation with reduced diffusion effects may be achieved by further optimisation of the seed layer and of the ferromagnetic layer.

Data availability statement

The data cannot be made publicly available upon publication because they are not available in a format that is sufficiently accessible or reusable by other researchers. The data that support the findings of this study are available upon reasonable request from the authors.

Acknowledgments

The authors would like to thank K O'Grady (University of York) for fruitful discussions. W Frost and G Vallejo-Fernandez would like to acknowledge EPSRC for funding the work (EP/V047779/1). Additionally R Carpenter would like to thank the process team at imec and the microscopy technicians for their contributions.

Author Contributions and Declarations

W F, R C and G V F wrote the main manuscript. R C produced the main samples. W F made the measurements. G V F fitted the data. All authors reviewed and contributed to editing and formatting the manuscript. The authors confirm there is no conflict of interest in relation to this publication.

ORCID iDs

W Frost https://orcid.org/0000-0001-5249-1006
G Vallejo-Fernandez https://orcid.org/0000-0002-4826-1547

References

[1] Sakhare S *et al* 2018 Enablement of STT-MRAM as last level cache for the high performance computing domain at the 5 nm node *IEEE Int. Electron Devices Meeting (IEDM)* p 18.3.1–4
[2] Lee K *et al* 2019 1 Gbit high density embedded STT-MRAM in 28nm FDSOI technology *IEEE Int. Electron Devices Meeting (IEDM)* p 2.2.1–4
[3] Fujita S, Noguchi H, Nomura K, Abe K, Kitagawa E, Shimomura N and Ito J 2013 Novel nonvolatile L1/L2/L3 cache memory hierarchy using nonvolatile-SRAM with voltage-induced magnetization switching and ultra low-write-energy MTJ *IEEE Trans. Magn.* **49** 4456–9
[4] Garello K *et al* 2019 Manufacturable 300 mm platform solution for field-free switching SOT-MRAM *Symp. on VLSI Technology* pp T194–5
[5] Grady K O, Fernandez-Outon L E and Vallejo-Fernandez G 2009 new paradigm for exchange bias in polycrystalline thin films *J. Magn. Magn. Mater.* **322** 883–99
[6] Vallejo-Fernandez G, Aley N P, Chapman J N and O'Grady K 2010 Measurement of the attempt frequency in antiferromagnets *Appl. Phys. Lett.* **97** 222505
[7] Baltz V, Manchon A, Tsoi M, Moriyama T, Ono T and Tserkovnyak Y 2018 Antiferromagnetic spintronics *Rev. Mod. Phys.* **90** 015005–1
[8] O'Grady K, Sinclair J, Elphick K, Carpenter R, Vallejo-Fernandez G, Probert M I and Hirohata A 2020 Anisotropy in antiferromagnets *J. Appl. Phys.* **128** 040901
[9] Wang Y *et al* 2023 Time-resolved detection of spin–orbit torque switching of magnetization and exchange bias *Nat. Electron.* **5** 840–8
[10] Oh Y-W *et al* 2016 Field-free switching of perpendicular magnetization through spin-orbit torque in antiferromagnet/ferromagnet/oxide structures *Nat. Nanotechnol.* **11** 878–84
[11] Lin P-H, Yang B-Y, Tsai M-H, Chen P-C, Chen K-F, Lin H-H and Lai C-H 2019 Manipulating exchange bias by spin–orbit torque *Nat. Mater.* **18** 335–41
[12] Kim Y K, Park G H, Lee S R, Min S H, Won J Y and Song S A 2003 Interface and microstructure evolutions in synthetic ferrimagnet-based spin valves upon exposure to postdeposition annealing *J. Appl. Phys.* **93** 7924–6
[13] Aley N P, Vallejo-Fernandez G, Kroeger R, Lafferty B, Agnew J, Lu Y and O'Grady K 2008 O'Grady, texture effects in IrMn/CoFe exchange bias systems *IEEE Trans. Magn.* **44** 2820–3
[14] Tsunoda M, Yoshitaki S, Ashizawa Y, Kim D Y, Mitsumata C and Takahashi M 2007 Enhancement of exchange bias by ultra-thin mn layer insertion at the interface of Mn-Ir/Co-Fe bilayers *Phys. Status Solidi* b **244** 4470–3
[15] Carpenter R, Cramp N C and O'Grady K 2012 Effect of Mn interface doping in polycrystalline exchange bias thin films *IEEE Trans. Magn.* **5** 4351–4
[16] Ali M, Marrows C H and Hickey B J 2008 Controlled enhancement or suppression of exchange biasing using impurity δ layers *Phys. Rev.* B **77** 134401
[17] Prejbeanu I L, Kerekes M, Sousa R C, Sibuet H, Redon O, Dieny B and Nozières J P 2007 Thermally assisted MRAM *J. Phys.: Condens. Matter* **19** 165218

[18] Ranjbar S, Tsunoda M, Oogane M and Ando Y 2019 Composition dependence of exchange anisotropy in PtMn/CoFe films *Jpn. J. Appl. Phys.* **58** 043001
[19] Ranjbar S, Al-Mahdawi M, Oogane M and Ando Y 2020 High-temperature magnetic tunnel junction magnetometers based on L10-PtMn pinned layer *IEEE Sens. Lett.* **4** 2500504
[20] Kato T, Ito H, Sugihara K, Tsunashima S and Iwata S 2004 Magnetic anisotropy of MBE grown MnPt3 and CrPt3 ordered alloy films *J. Magn. Magn. Mater.* **272–276** 778–9
[21] Vallejo-Fernandez G, Fernandez-Outon L E and O'Grady K 2007 Measurement of the anisotropy constant of antiferromagnets in metallic polycrystalline exchange biased systems *Appl. Phys. Lett.* **91** 212503
[22] Lawrence R A, Donaldson S J and Probert M I 2023 Magnetic transition state searching: beyond the static ion approximation *Magnetochemistry* **9** 42
[23] Fernandez-Outon L E, Vallejo-Fernandez G, Manzoor S, Hillebrands B and O'Grady K 2008 O'Grady, interfacial spin order in exchange biased systems *J. Appl. Phys.* **104** 093907
[24] Fernandez-Outon L E, O'Grady K, Sangmun O, Zhou M and Pakala M 2008 Large exchange bias IrMn/CoFe for magnetic tunnel junctions *IEEE Trans. Magn.* **44** 2824–7
[25] Gaunt P 1986 Magnetic viscosity and thermal activation energy *J. Appl. Phys.* **591** 245–2544
[26] Krén E, Kádár G, Pál L, Sólyom J, Szajbó P and Tarnóczi T 1968 Magnetic structures and exchange interactions in the Mn-Pt system *Phys. Rev.* **171** 574–85
[27] Ji C X, Ladwig P F, Ott R D, Yang Y, Yang J J, Chang Y A, Linville E S, Gao J and Pant B B 2006 An investigation of phase transformation behavior in sputter-deposited Maps thin films *JOM* **58** 50–54
[28] Pál L, Krén E, Kádár G, Szabó P and Tarnóczi T 1968 Magnetic structures and phase transformations in Mn-based CuAu-I type alloys *J. Appl. Phys.* **39** 538–44
[29] Farkas D 2021 Varying diffusion kinetics along random grain boundaries in a model austenitic stainless steel *Metall. Mater. Trans.* A **52** 1117–26
[30] Patterson A L 1939 The Scherrer formula for x-ray particle size determination *Phys. Rev.* **56** 978–82
[31] Naik V B *et al* 2020 JEDEC-qualified highly reliable 22 nm FD-SOI embedded MRAM for low-power industrial-grade and extended performance towards automotive-grade-1 applications *Technical Digest–Int. Electron Devices Meeting, IEDM 2020-December* p 11.3.1–4